

Article

Coherent Resonant Soft X-ray Scattering Study of Magnetic Textures in FeGe

Victor Ukleev ^{1,*}, Yuichi Yamasaki ^{1,2,3}, Daisuke Morikawa ¹, Naoya Kanazawa ⁴,
Yoshihiro Okamura ⁴, Hironori Nakao ⁵, Yoshinori Tokura ^{1,4} and Taka-hisa Arima ^{1,6}

¹ RIKEN Center for Emergent Matter Science (CEMS), Wako 351-0198, Japan;

yuichi.yamasaki@riken.jp or yamasaki.yuichi@nims.go.jp (Y.Y.); d-morikawa@riken.jp (D.M.);
tokura@riken.jp (Y.T.); takahisa.arima@riken.jp (T.A.)

² Research and Services Division of Materials Data and Integrated System (MaDIS), National Institute for
Materials Science (NIMS), Tsukuba 305-0047, Japan

³ PRESTO, Japan Science and Technology Agency (JST), Kawaguchi 332-0012, Japan;

⁴ Department of Applied Physics and Quantum-Phase Electronics Center (QPEC), University of Tokyo,
Tokyo 113-8656, Japan; kanazawa@ap.t.u-tokyo.ac.jp (N.K.); okamura@cmr.t.u-tokyo.ac.jp (Y.O.)

⁵ Condensed Matter Research Center and Photon Factory, Institute of Materials Structure Science,
High Energy Accelerator Research Organization, Tsukuba 305-0801, Japan; hironori.nakao@kek.jp

⁶ Department of Advanced Materials Science, University of Tokyo, Kashiwa 277-8561, Japan

* Correspondence: victor.ukleev@riken.jp

Received: 19 September 2017; Accepted: 15 January 2018; Published: 19 January 2018

Abstract: Coherent resonant soft X-ray scattering was utilized to examine the magnetic textures in a thin plate of the cubic B20 compound FeGe. Small-angle scattering patterns were measured with controlled temperatures and magnetic fields exhibiting magnetic scattering from a helical texture and skyrmion lattice. By measuring the scattering pattern in a saturation magnetic field, magnetic and charge scattering were distinguished and an iterative phase retrieval algorithm was applied to reconstruct the magnetic texture in the real-space. Results of the real-space reconstruction of magnetic texture from two independently measured datasets were used to compare the reliability of the retrieval.

Keywords: resonant soft X-ray scattering; coherent diffraction imaging; skyrmions

PACS Classification: 61.05.cf; 61.05.cj; 75.25.-j; 42.30.Rx

1. Introduction

Lensless imaging with coherent hard and soft X-rays is a rapidly developing technique, which has been successfully performed in various studies in the fields of nanotechnology, biology, and condensed matter physics [1]. The method is extremely useful for the structural examination of non-crystalline specimens [1–4], and can be applied for the determination of the exact positions of individual scattering objects and the mapping of defects in periodically ordered structures [5,6]. One of the promising applications of coherent soft X-rays is the imaging of the local magnetization of magnetic specimens [7]. In the soft X-ray regime, by exciting electrons from the 2p state to the 3d state of transition-metal atoms, it is possible to study the magnetic ordering in wide-angle diffraction [8–10] or small-angle scattering geometry [11–15]. Moreover, a topological winding number of the magnetically ordered system can be directly determined from the polarization-dependent (or dichroic) soft X-ray diffraction pattern alone [16]. Dichroic resonant soft X-ray scattering can be successfully combined with coherent diffraction approaches such as iterative phase retrieval [17–19], Fourier transform holography-based methods [20–23], and ptychography [24,25] for the lensless real-space imaging

of local magnetic moment at the scale from a few tens of nanometers to a few microns. Lensless approaches allow the use of various sample environments, which confers a significant advantage compared to zone-plate-based magnetic transmission X-ray microscopy. Coherent diffraction allows the solution of classical crystallographic inverse problems of phase retrieval by using the iterative reconstruction algorithms applied to diffraction intensities, which are proportional only to the modulus of the complex Fourier transform of the scattering function. In principle, the resolution of an image obtained by means of the phase retrieval algorithm is limited only by the highest spatial frequency contained in the diffraction pattern. However, noise, instabilities of the sample and experimental setup, radiation damage, missing pixels due to a beamstop shadow, etc. can possibly limit the achievable contrast and spatial resolution [3,26,27]. In order to find a unique solution to the phase problem, phase retrieval algorithms need a priori knowledge, such as a fixed region around the sample characterized by zero scattering (known support), positivity, and reality constraints [28,29]. For example, Fienup's hybrid input-output (HIO) [30] is one of the most effective algorithms for coherent X-ray diffraction imaging which employs measured diffraction pattern and guess of the sample shape to iteratively reconstruct the sample real-space image [29]. The Shrinkwrap algorithm can be used when the tight support is unknown to determine the sample shape directly from the Patterson function [31].

In the present paper, we employed a phase retrieval algorithm to reconstruct the lensless images of the magnetic textures from the coherent small-angle resonant soft X-ray scattering (RSXS) patterns measured from the magnetically ordered compound FeGe. The magnetic phase diagram of B20-type non-centrosymmetric cubic FeGe has been extensively studied for bulk crystals [32,33], thin plates [14,34], and epitaxial films [35–40]. Helical magnetic ordering appears in FeGe at zero field near room temperature ($T_c = 280$ K) due to the interplay between exchange interaction, Dzyaloshinskii–Moriya interaction, and anisotropy [41]. By application of the moderate magnetic field in a range between $B = 50$ and 100 mT, the helical structure can be transformed to the ordered lattice of topologically protected vortex-like spin configurations, a magnetic skyrmion crystal (SkX) [33,34]. Similar to the Abrikosov vortices in type-II superconductors, SkX tends to form a (single- or multi-domain) triangular lattice. In the past decade, SkX has been observed in bulk crystals of chiral B20 compounds by means of small-angle neutron scattering [33,42,43]. Alternatively, Lorentz transmission electron microscopy (LTEM) has been employed for the real-space imaging of SkX in thin plates [34,44]. On the other hand, recent developments of the synchrotron radiation sources and X-ray free-electron laser facilities provide several advantages to X-ray methods over the neutron scattering and electron microscopy: high brilliance of the X-ray sources, wide energy range, spatial coherence, and short time length of the pulses. The typical characteristic lengthscale of the skyrmion lattice in B20 compounds ranges from a few tens to hundreds of nanometers, which corresponds to the small-angle scattering region for the soft X-rays with energies matching the $L_{2,3}$ absorption edges of transition metals. Furthermore, soft X-ray imaging is a complementary technique to LTEM which is sensitive to the in-plane magnetic flux inside the sample and produces no contrast in the case of Néel-type skyrmions [45–47], which has been recently observed in magnetic ultra-thin films [48–50] and bulk polar magnets [51–54].

2. Materials and Methods

2.1. Simulation of the Noise and Beamstop Effect on the Phase Retrieval Reliability

Experiments on the small-angle X-ray scattering in transmission geometry often require the introduction of a beamstop to protect the detector from the transmitted direct beam. Moreover, for soft X-rays, the complication of the all-vacuum environment is lifted, and it is not always possible to control the dynamical range of the measured diffraction intensity by changing the sample-detector and beamstop-detector distances. Therefore, in order to evaluate the possibility of the real-space reconstruction from the coherent small-angle diffraction pattern in the case when a certain amount

of central pixels are missing due to the beamstop shadow, a simulation with an artificial dataset was first performed.

A problem for accurate reconstruction occurs when the measured scattering pattern contains regions with missing data, even when the oversampling condition is satisfied and tight support is known. As has been shown previously [26,27,55] by numerical simulations, the incorrect support and the missing area at the center of the diffraction pattern can drastically reduce the real-space reconstruction quality. However, the effect of a beamstop can be potentially reduced in cases where the scattering signal from a periodic structure of the sample is isolated in a limited region of Fourier space (it may also be called reciprocal- or q -space). We numerically investigated the robustness of the HIO algorithm on missing pixels in this case. The real-space image of 650×650 pixels (px) used for the test was a scanning electron microscopy (SEM) photograph of the ordered monolayer of metallic nanoparticles (Figure 1a) with a chosen asymmetric mask. Gaussian background noise of a magnitude comparable to the second-order Bragg reflections was added to the Fourier transform modulus of the original image. To simulate the subtraction of the charge scattering from the RSXS data, the contour of the asymmetric mask in the original image was isolated and the corresponding Fourier transform was subtracted from the scattering pattern. Furthermore, a circular “beamstop” with radius of $R = 10, 20, 30, 40,$ or 50 pixels was introduced to remove the central pixels (Figure 1e). The resultant intensity distribution was employed for the iterative phase retrieval using the HIO algorithm with enforced reality and positivity constraints, known support, and the feedback parameter $\beta = 0.9$. The algorithm was stagnating to the local minima after 200 iterations; 100 individual trials were averaged. Results of the reconstructions with the beamstops of $R = 0, 20,$ and 50 pixels are shown in Figure 1b–d, respectively. The two-dimensional hexagonal lattice in the original image contains a few packing defects (Figure 1a), which can be clearly reproduced only when the beamstop radius is smaller than four pixels, while for $R \geq 4$ px these defects are almost vanished. Fourier ring correlation (FRC) analysis has been used to summarize the influence of the missing central pixels on the reconstruction quality [56,57] (Figure 1f). The FRC measures the spatial frequency dependence of the cross-correlation of the Fourier transform intensity from two independently reconstructed datasets. The resolution is calculated at the point where the FRC curves irreversibly cross the $1/2$ threshold [56]. The resultant real-space resolution of a reconstructed image decreases from 4 px to 6 px as the missing area radius increases from $R = 10$ px to $R = 50$ px; in the latter case, the resolution is comparable with the average radius of nanoparticles shown in the original image. The overall contrast is drastically reduced as the pixels at the center are removed. Nevertheless, the positions of the scatterers in the lattice are determined correctly, while sizes and shapes of individual nanoparticles are lost.

If the background noise is higher than the intensity of the second-order Bragg peaks, the smooth brightness variation on the scale of an individual object in the original picture is eventually replaced by a sharp drop of brightness intensity at the center of each nanoparticle. A similar effect can be observed if the intensity in the q -space region outside the six first-order Bragg peaks is removed. In this situation, the form factor of the object in the lattice is sampled by only a few points in reciprocal space (at the structural Bragg peaks positions) and modulates the intensities of the corresponding peaks. Experimentally, similar results have been unambiguously demonstrated in [5], where exclusion of the higher-order harmonics from the input Fourier-space pattern resulted in the loss of information about the individual shape and size of the nanograins in the photonic crystal superlattice. Therefore, when the measured diffraction pattern is limited in q -space by first-order Bragg peaks, only reconstruction of the pinhole shape and particle positions can be retrieved. To summarize, our present simulation suggests that if the support is known, the information about the coordinates of the scatterers in the ordered lattice can be retrieved from the coherent small-angle scattering data—even in the case when almost all central pixels between the first-order Bragg peaks are missing. In order to get rid of the data contamination by the beamstop shadow, one should consider the use of multiple expositions taken with different beamstop positions to increase the effective dynamic range [58], employ a semi-transparent beamstop [59], or substitute missing pixels with the intensity measured near the transmitted beam

with the absorption filter [60]. Unfortunately, none of these methods could be applied in the present experimental setup.

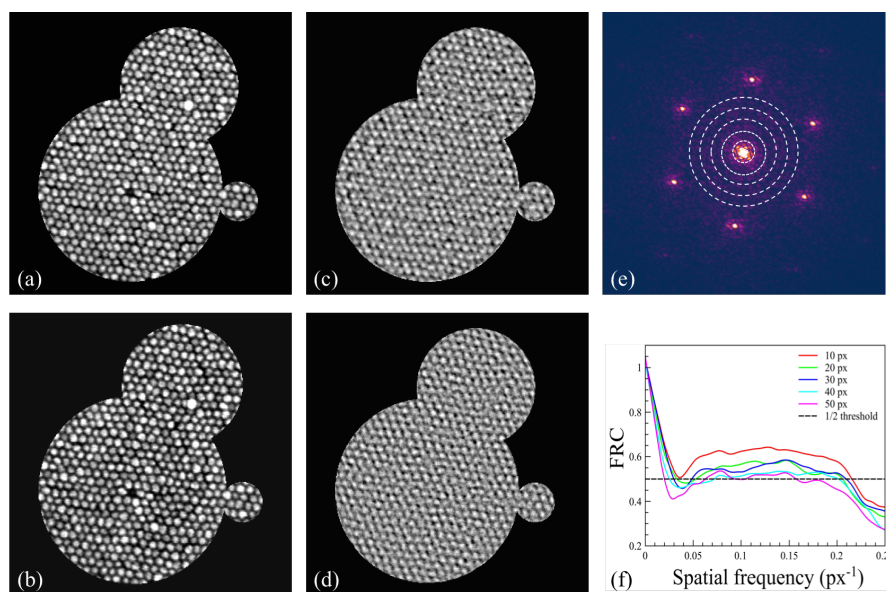


Figure 1. Numerical investigation of the robustness of the hybrid input-output (HIO) algorithm: (a) original image; reconstructions obtained from the square root of the modulus of the Fourier transform of the original image when central area with radius (b) $R = 0$; (c) $R = 20$; (d) $R = 50$ pixels (px) were removed. (e) Fourier transform of the original image (a); dashed white lines indicate the beamstop area. (f) Fourier ring correlation (FRC) analysis of the reconstructed images.

2.2. Experiment

The RSXS experiment was carried out at the soft X-ray undulator beamline BL-16A, Photon Factory, KEK, Tsukuba, Japan. The setup is equipped with a high-vacuum chamber with a background pressure of 10^{-8} Torr. The scattered intensity was collected by an in-vacuum charge coupled device (CCD) detector (512×512 pixels, Princeton Instruments, Trenton, NJ, USA) protected from the transmitted X-ray beam by a tungsten beamstop with a size of ~ 0.2 – 0.3 mm situated at the fixed distance in front of the CCD matrix. A magnetic field \mathbf{B} produced by a Helmholtz coil up to 400 mT was applied parallel to the incident X-ray and perpendicular to the sample plane. A He-flow-type refrigerator was used to control the sample temperature. The cryostat is equipped with a heater for temperature control in the range from 15 K to 320 K [61].

The experiment was performed with a single-crystalline thin plate of FeGe using soft X-rays at the resonant energy $E = 707$ eV corresponding to the L_3 absorption edge of iron. Since the X-ray attenuation length for FeGe at this edge is $l_a \approx 120$ nm, a plate with a thickness of $l = 200$ nm was prepared by focused ion beam (FIB) milling and fixed to a Si_3N_4 membrane by a tungsten contact. The back side of the membrane was coated with a ~ 4 μm Au absorbing layer to protect the detector from the transmitted X-ray beam. An SEM image of the sample aperture produced in the gold mask by FIB is shown in Figure 2a from the front (silicon nitride) side. The asymmetric shape of the pinhole was chosen to provide better stagnation and verify the reliability of the phase retrieval algorithm [28]. The aperture size was chosen based on the longitudinal coherence length of the X-ray beam (10 μm) to satisfy the oversampling condition. The dark-gray area around the aperture shown in Figure 2a is the remaining silicon nitride layer, which was not removed completely by the etching routine, but nevertheless was almost transparent to the incoming X-rays. To prevent the contamination of the specimen by Ga^+ ions during the FIB milling process, the thin plate of FeGe was attached to the back side of the membrane after fabrication of the sample aperture (Figure 2b).

The X-ray scattering factor for resonant magnetic scattering can be expressed by the equation:

$$\mathbf{f} = (\mathbf{e} \cdot \mathbf{e}')\mathbf{f}_c + i(\mathbf{e} \times \mathbf{e}') \cdot \mathbf{M}\mathbf{f}_m^1 + (\mathbf{e} \cdot \mathbf{M})(\mathbf{e}' \cdot \mathbf{M})\mathbf{f}_m^2, \quad (1)$$

where \mathbf{e} and \mathbf{e}' are polarization vectors of the incident and scattered photons, respectively; \mathbf{f}_c is the transition matrix element corresponding to the charge scattering; \mathbf{M} is the magnetization; \mathbf{f}_m^1 and \mathbf{f}_m^2 are attributed to the magnetic scattering. The second term $i(\mathbf{e} \times \mathbf{e}') \cdot \mathbf{M}\mathbf{f}_m^1$ changes sign for incident photons with opposite (right circular (RC) and left circular (LC)) polarizations. The third term containing \mathbf{f}_m^2 is quadratic in the magnetization and much smaller compared to the first two terms in case of the $L_{2,3}$ edge of transition metals [62]. The experimentally measured intensity I_m is equal to the squared Fourier transform of the complex scattering factor \mathbf{f} and consists of charge scattering, magnetic scattering, and their interference.

Two-dimensional RSXS datasets obtained with circularly polarized X-rays at temperature $T = 280$ K and applied magnetic fields $B = 0$ mT, $B = 50$ mT, and $B = 220$ mT are shown in Figure 3. The data acquisition time was 1 s, and a series of 100 frames was summed to maximize the scattering signal for each field condition. The “golf club”-shaped region at the center of the diffraction patterns is the beamstop shadow. The parasite scattering signal arising from imperfections of gold coating and sample aperture is manifested as the intense rays diverging from the center of the pattern in Figure 3a–c. This background scattering was isolated by measurement of the RSXS pattern in the field-polarized (spin-collinear) state of FeGe at the applied field of $B = 220$ mT (Figure 3c). Alternatively, the charge scattering alone can be measured in off-resonance condition by tuning the incident X-rays' energy and subtracting from the pattern after appropriate normalization.

Small-angle scattering from a helical magnetic structure can be clearly observed at zero magnetic field (Figure 3a) as two symmetric Bragg peaks corresponding to the single-domain helical state with real-space periodicity $\lambda_h = 73$ nm. A similar periodicity of magnetic structure $\lambda_{SkX} = 73$ nm can be observed for SkX state (Figure 3b) when a magnetic field of $B = 50$ mT is applied. We can suggest that the inequality between the skyrmion and the helical texture periodicities in FeGe samples reported in a previous resonant soft X-ray scattering experiment ($\lambda_h = 68$ nm while $\lambda_{SkX} = 73$ nm) [14] has been induced by the tensile strain due to the tungsten contacts that were used to attach the specimen to the Si_3N_4 substrate [63]. In the present setup, we used a strain-free sample which was fixed to the membrane by only one tungsten contact (Figure 2b). Thus, the resultant periodicity of the helical and skyrmion textures $\lambda_h = \lambda_{SkX} = 73$ nm match each other and the previously reported values for the thin FeGe plates [34]. For the higher fields ($B > 120$ mT), the magnetic small-angle scattering was not observed (Figure 3c) in the present q range due to the field-polarized state of FeGe.

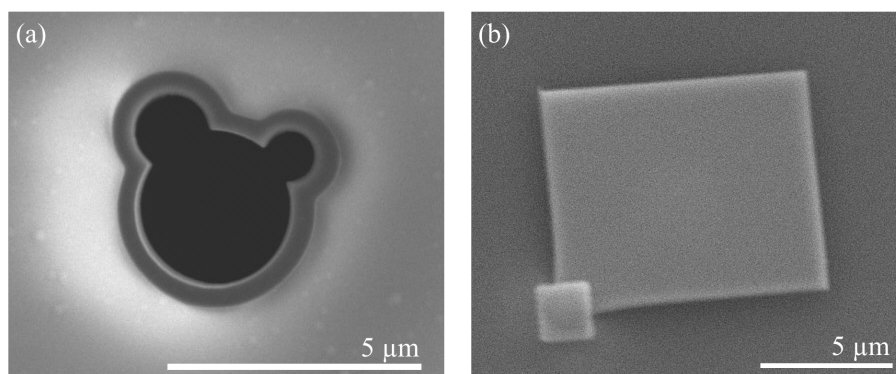


Figure 2. (a) Scanning electron microscopy (SEM) image of the sample aperture; (b) FeGe thin plate fixed on the opposite side of Si_3N_4 membrane by a tungsten contact.

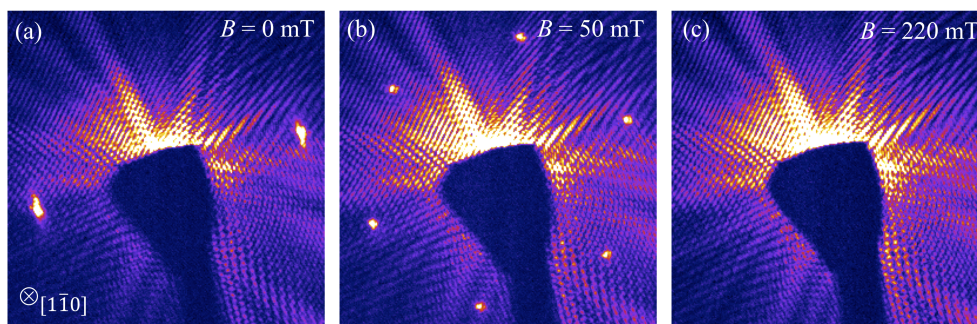


Figure 3. Resonant soft X-ray scattering (RSXS) patterns measured at $T = 280$ K and (a) $B = 0$ mT corresponding to the helical phase of FeGe; (b) $B = 50$ mT corresponding to the skyrmion crystal (SkX) phase; and (c) field-polarized state at $B = 220$ mT.

3. Results and Discussion

The real-space image of the sample aperture has been retrieved by a Shrinkwrap algorithm [31] from RSXS patterns measured in the field-polarized state (Figure 3c). The obtained pinhole size, shape, and orientation delivered by the reconstruction were in good agreement with SEM images. The shape of the reconstructed aperture suggests that the dark-gray area around the hole (Figure 2a) is transparent to the X-rays, indicating that the thickness of the remaining silicon nitride layer is negligible. Further, the sample shape shown in Figure 4a was used as the object-plane support domain constraint for the phase-retrieval algorithm applied to the data measured at $B = 0$ mT and $B = 50$ mT. Due to the large difference between the spatial frequencies and overall decay of small-angle scattering intensity functions, we considered that the interference between magnetic and charge scattering is negligible [64]. Furthermore, the charge scattering was subtracted from the datasets taken at $B = 0$ mT, $B = 50$ mT in order to isolate the magnetic contributions. The residual diffraction pattern intensity is proportional to the absolute square of Fourier transform of the magnetization density. Therefore, the square root of the measured intensity $\sqrt{I_m}$ was used as real part of the Fourier-space constraint for the phase retrieval algorithm. The central pixels that were hidden by the beamstop shadow ($|q| < 0.08 \text{ \AA}^{-1}$) were allowed to vary freely. The resultant magnetic RSXS patterns were employed for the phase retrieval. We used the HIO algorithm with improved noise tolerance [65] and did not assume positivity nor reality constraints. Reconstructed images obtained by 1000 individual runs of the algorithm with random initial phases were averaged. The bi-cubic interpolation was applied to the resultant images.

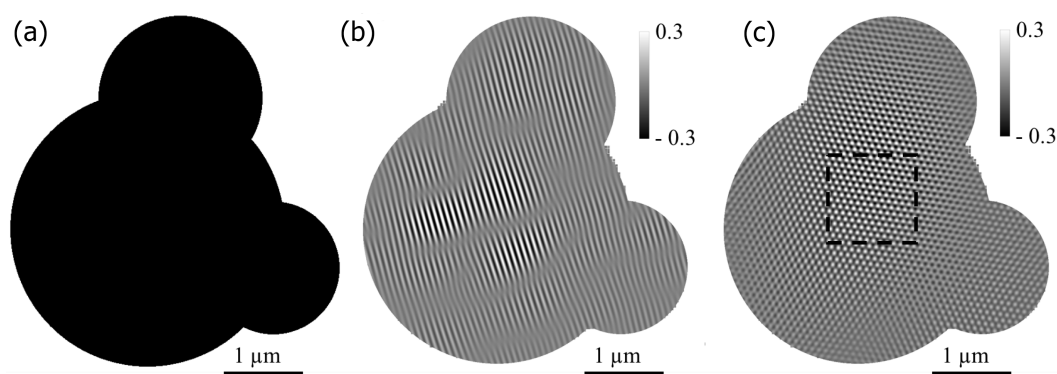


Figure 4. (a) Real-space support used for iterative phase retrieval; (b) Imaginary part of the reconstruction of the magnetic texture of FeGe at $B = 0$ mT (helical phase) and (c) $B = 50$ mT (SkX phase). The grayscale bar is given in arbitrary units. The black rectangle in panel (c) indicates the magnification area shown in Figure 5.

The binary image of the sample support is shown in Figure 4a. Imaginary parts of the reconstructed complex-valued images of the helical texture and skyrmion lattice shown in Figure 4b,c are obtained from RSXS patterns (Figure 3a,b) measured at $B = 0$ mT and $B = 50$ mT, respectively, by the algorithm described above. The magnetic scattering intensity was maximized at the energy $E = 707$ eV, providing maximal contrast for the real part of the transmission function, which is proportional to the local spin density. Considering the subtraction of the charge scattering from the diffraction patterns, the real-space contrast in Figure 4b,c is directly proportional to the projection of the magnetization along the field direction. Fluctuations of the brightness represented as white blur in Figure 4b,c can be ascribed to the residual charge scattering from the specimen roughness, random low-frequency modulation due to the missing speckles, charge and magnetic scattering interference, and other experimental or calculation issues. As discussed in Section 2.1, since only the first-order Bragg peaks are present in the diffraction pattern, the real-space reconstruction of the particles' positions but not the form-factor can be retrieved. We attribute the appearance of the black and white dot variation seen in Figure 4c only to the deformation of the particles' shape, since it does not break the periodic function delivered by the structure factor.

The magnification of the area highlighted in the black box in Figure 4c is shown in Figure 5. Figure 5a,b corresponds to the real-space images independently reconstructed from the datasets measured with LC (Figure 5a) and RC (Figure 5b) polarizations. Note, that in this case the full patterns containing the charge and parasitic scattering were used as an input intensities. The images obtained by phase retrieval are unclear; nevertheless, a hexagonally-ordered array of spots is visible. Moreover, the contrast inverts at the spots positions between the opposite polarizations, indicating their magnetic origin. However, the quality of the images is poor. We suggest that reconstructions of full scattering patterns do not deliver clear contrast due to the contribution of the parasitic charge scattering, making the images unreproducible between the different runs of the algorithm and therefore cannot be assigned to the real charge modulations, such as a roughness of the thin plate. Especially in the RC polarization case, the contrast in the reconstructed images is more blurred compared to the LC. We attribute this effect to the small shift of the photon energy and position of the RC-polarized beam compared to LC, resulting in the reduced signal-to-noise ratio. Consequently, the isolation of magnetic scattering was performed by subtracting the diffraction pattern measured at the field-polarized state ($B = 220$ mT) from the patterns measured at $B = 0$ and $B = 50$ mT. Simulation (Section 2.1) suggests that ordered texture determination is not significantly affected by this routine. By subtracting the charge scattering in the reciprocal space, the quality of the reconstruction can be improved drastically (Figure 5c,d). Meanwhile the real-space difference pattern between RC and LC reconstructions contain the magnetic real-space contrast; the sum, in principle, should provide a charge density distribution [25]. However, subtraction of the charge scattering from the Fourier-space patterns excludes this possibility. Therefore, to enhance the magnetic contrast, the difference between two reconstructions from datasets measured with LC- and RC-polarized photons were taken (Figure 5e,f). Indeed, by comparing the positions of skyrmions in the lattice and magnetization direction of the cores and the outer parts of skyrmions for the images reconstructed from the data taken with opposite polarizations, one can conclude the reliability of the real-space image. When the helicity of the X-ray beam is changed from left to right, the sign of the term $i(\mathbf{e} \times \mathbf{e}') \cdot \mathbf{Mf}_m^1$ in Equation (1) and real-space magnetic contrast invert. Consequently, we can observe a clear magnetic texture in the difference patterns resulted from the subtraction of two real-space images retrieved from the datasets taken with LC and RC polarizations (Figure 5e,f).

The resolution threshold of the reconstruction is determined by the highest measured Fourier harmonics, and can be improved by measuring higher-order Bragg reflections. We did not apply any commonly used phase-retrieval transfer function or the Fourier ring correlation analysis due to the a priori known limited q -range of magnetic scattering. Alternatively, the reliability of the single reconstructed magnetic pattern can be examined by means of a Gabor transform, as has been proposed by Flewett et al. [18]. In the present study, we used real-space textures reconstructed from the RSXS

patterns taken with RC- and LC-polarized photons at the same sample conditions to qualitatively evaluate the reliability. We can determine the position of each skyrmion by the template-matching method via normalized cross-correlation function (CCF) [66]. The matching pixels of the template and the tested image would be identified by a peak in the CCF. Therefore, the coordinates of each skyrmion particle at the reconstructed pattern can be identified and compared for both reconstructions. Thus by using one skyrmion as the template and comparing the coordinates of templates for each real-space pattern, we can conclude that the real-space error (displacement of the individual skyrmions) does not exceed 40 nm. Therefore, we can assign this unit cell displacement as a real-space resolution of the reconstructed image. This number can be improved by measuring the higher-order scattering harmonics with a good statistics what will allow a form factor of the individual vortices to be obtained.

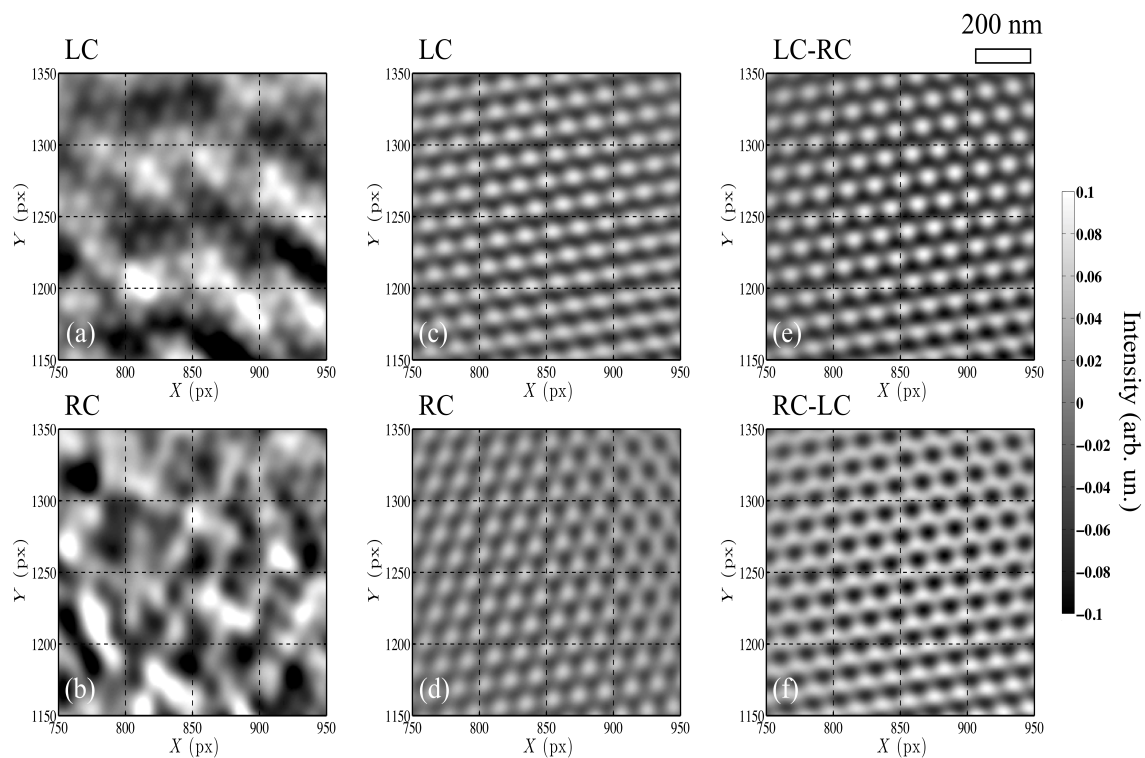


Figure 5. Magnification of the real-space image of the skyrmion lattice obtained by the iterative phase retrieval. Patterns shown in panels (a,b) are reconstructed from the square root of the original RSXS data obtained with left circular (LC) and right circular (RC) soft X-ray polarizations, respectively; (c) Real-space reconstruction of the LC and (d) RC datasets were processed as described in Section 2.2; (e) Difference of left and right polarized reconstructed images (LC-RC) and (f) right and left (RC-LC) reconstructions showing the contrast inversion for opposite polarizations. The axis values are given in pixels for the convenient determination of the positions of the vortices.

4. Conclusions

In conclusion, we have probed the magnetic texture of FeGe by means of coherent small-angle scattering with circularly polarized soft X-rays. We have performed the first to our knowledge lensless imaging of an ordered magnetic texture with in-situ controlled temperature and magnetic field using an iterative phase retrieval approach. The method can be used with both circularly and linearly polarized soft X-ray beams, and does not require any focusing X-ray optics to perform magnetic imaging with a resolution of a few tens of nanometers, and therefore allows the use of various sample environments. Coherent small-angle resonant soft X-ray scattering can be applied to a wide range of further experiments, including the investigation of Néel-type skyrmion compounds and time-resolved

studies of skyrmion textures in both Fourier and real-space. Moreover, phase retrieval can be employed as a supplementary technique for resonant small-angle scattering and Bragg diffraction; for example, it can improve the scanning-based technique of mapping skyrmion domains in continuous samples [10] by masking the incoming X-ray beam by a pinhole.

Acknowledgments: This research was supported in part by PRESTO Grant Number JPMJPR177A from Japan Science and Technology Agency (JST), “Materials research by Information Integration” Initiative (MI²I) project of the Support Program for Starting Up Innovation Hub from JST, the Japan Society for the Promotion of Science through the Funding Program for World-Leading Innovative R&D on Science and Technology (FIRST Program), and JSPS KAKENHI Grant Number 16H05990. Soft X-ray scattering experiments at KEK Photon Factory were performed as a part of the Project No.: 2015S2-007.

Author Contributions: Y.T. and T.A. jointly conceived the project. The single crystal growth was performed by N.K. and FIB processing was performed by D.M. Soft X-ray scattering experiment was carried out by V.U., Y.Y., Y.O. and H.N. Iterative phase retrieval, simulations and manuscript preparation were done by V.U. The results were discussed and interpreted by all authors.

Conflicts of Interest: The authors declare no conflict of interest. The founding sponsors had no role in the design of the study; in the collection, analyses, or interpretation of data; in the writing of the manuscript, and in the decision to publish the results.

References

1. Miao, J.; Ishikawa, T.; Robinson, I.K.; Murnane, M.M. Beyond crystallography: Diffractive imaging using coherent X-ray light sources. *Science* **2015**, *348*, 530–535.
2. Miao, J.; Charalambous, P.; Kirz, J.; Sayre, D. Extending the methodology of X-ray crystallography to allow imaging of micrometre-sized non-crystalline specimens. *Nature* **1999**, *400*, 342–344.
3. Tuchin, V.V. Handbook of coherent-domain optical methods. In *Handbook of Coherent-Domain Optical Methods: Biomedical Diagnostics, Environmental Monitoring, and Materials Science*; Springer Science+Business Media: New York, NY, USA, 2013; ISBN 978-1-4614-5175-4.
4. Chapman, H.N.; Nugent, K.A. Coherent lensless X-ray imaging. *Nat. Photonics* **2010**, *4*, 833–839.
5. Gulden, J.; Yefanov, O.; Mancuso, A.; Abramova, V.; Hilhorst, J.; Byelov, D.; Snigireva, I.; Snigirev, A.; Petukhov, A.; Vartanyants, I. Coherent x-ray imaging of defects in colloidal crystals. *Phys. Rev. B* **2010**, *81*, 224105.
6. Gulden, J.; Yefanov, O.; Mancuso, A.; Dronyak, R.; Singer, A.; Bernátová, V.; Burkhardt, A.; Polozhentsev, O.; Soldatov, A.; Sprung, M.; et al. Three-dimensional structure of a single colloidal crystal grain studied by coherent X-ray diffraction. *Opt. Express* **2012**, *20*, 4039–4049.
7. Fischer, P. X-ray imaging of magnetic structures. *IEEE Trans. Magn.* **2015**, *51*, 1–31.
8. Wilkins, S.; Hatton, P.; Roper, M.; Prabhakaran, D.; Boothroyd, A. Soft X-ray resonant magnetic diffraction. *Phys. Rev. Lett.* **2003**, *90*, 187201.
9. Langner, M.; Roy, S.; Mishra, S.; Lee, J.; Shi, X.; Hossain, M.; Chuang, Y.D.; Seki, S.; Tokura, Y.; Kevan, S.; et al. Coupled skyrmion sublattices in Cu₂OSeO₃. *Phys. Rev. Lett.* **2014**, *112*, 167202.
10. Zhang, S.; Bauer, A.; Burn, D.M.; Milde, P.; Neuber, E.; Eng, L.M.; Berger, H.; Pfeleiderer, C.; van der Laan, G.; Hesjedal, T. Multidomain Skyrmion Lattice State in Cu₂OSeO₃. *Nano Lett.* **2016**, *16*, 3285–3291.
11. Tonnerre, J.; Seve, L.; Raoux, D.; Soullié, G.; Rodmacq, B.; Wolfers, P. Soft X-ray resonant magnetic scattering from a magnetically coupled Ag/Ni multilayer. *Phys. Rev. Lett.* **1995**, *75*, 740.
12. Gutt, C.; Streit-Nierobisch, S.; Stadler, L.M.; Pfau, B.; Günther, C.; Könnecke, R.; Frömter, R.; Kobs, A.; Stickler, D.; Oepen, H.; et al. Single-pulse resonant magnetic scattering using a soft X-ray free-electron laser. *Phys. Rev. B* **2010**, *81*, 100401.
13. Kortright, J.B.; Kim, S.K.; Denbeaux, G.P.; Zeltzer, G.; Takano, K.; Fullerton, E.E. Soft-X-ray small-angle scattering as a sensitive probe of magnetic and charge heterogeneity. *Phys. Rev. B* **2001**, *64*, 092401.
14. Yamasaki, Y.; Morikawa, D.; Honda, T.; Nakao, H.; Murakami, Y.; Kanazawa, N.; Kawasaki, M.; Arima, T.; Tokura, Y. Dynamical process of skyrmion-helical magnetic transformation of the chiral-lattice magnet FeGe probed by small-angle resonant soft X-ray scattering. *Phys. Rev. B* **2015**, *92*, 220421.
15. Okamura, Y.; Yamasaki, Y.; Morikawa, D.; Honda, T.; Ukleev, V.; Nakao, H.; Murakami, Y.; Shibata, K.; Kagawa, F.; Seki, S.; et al. Directional electric-field induced transformation from skyrmion lattice to distinct helices in multiferroic Cu₂OSeO₃. *Phys. Rev. B* **2017**, *95*, 184411.

16. Zhang, S.; Van Der Laan, G.; Hesjedal, T. Direct experimental determination of the topological winding number of skyrmions in Cu_2OSeO_3 . *Nat. Commun.* **2017**, *8*, doi:10.1038/ncomms14619.
17. Turner, J.J.; Huang, X.; Krupin, O.; Seu, K.A.; Parks, D.; Kevan, S.; Lima, E.; Kisslinger, K.; McNulty, I.; Gambino, R.; et al. X-ray diffraction microscopy of magnetic structures. *Phys. Rev. Lett.* **2011**, *107*, 033904.
18. Flewett, S.; Schaffert, S.; Mohanty, J.; Guehrs, E.; Geilhufe, J.; Günther, C.M.; Pfau, B.; Eisebitt, S. Method for single-shot coherent diffractive imaging of magnetic domains. *Phys. Rev. Lett.* **2012**, *108*, 223902.
19. Flewett, S.; Günther, C.; von Korff Schmising, C.; Pfau, B.; Mohanty, J.; Büttner, F.; Riemeier, M.; Hantschmann, M.; Kläui, M.; Eisebitt, S. Holographically aided iterative phase retrieval. *Opt. Express* **2012**, *20*, 29210–29216.
20. Eisebitt, S.; Lüning, J.; Schlotter, W.; Lörger, M.; Hellwig, O.; Eberhardt, W.; Stöhr, J. Lensless imaging of magnetic nanostructures by X-ray spectro-holography. *Nature* **2004**, *432*, 885–888.
21. Scherz, A.; Schlotter, W.; Chen, K.; Rick, R.; Stöhr, J.; Lüning, J.; McNulty, I.; Günther, C.; Radu, F.; Eberhardt, W.; et al. Phase imaging of magnetic nanostructures using resonant soft X-ray holography. *Phys. Rev. B* **2007**, *76*, 214410.
22. Pfau, B.; Günther, C.M.; Könecke, R.; Guehrs, E.; Hellwig, O.; Schlotter, W.F.; Eisebitt, S. Magnetic imaging at linearly polarized x-ray sources. *Opt. Express* **2010**, *18*, 13608–13615.
23. Duckworth, T.A.; Ogrin, F.; Dhesi, S.S.; Langridge, S.; Whiteside, A.; Moore, T.; Beutier, G.; Van Der Laan, G. Magnetic imaging by X-ray holography using extended references. *Opt. Express* **2011**, *19*, 16223–16228.
24. Tripathi, A.; Mohanty, J.; Dietze, S.H.; Shpyrko, O.G.; Shipton, E.; Fullerton, E.E.; Kim, S.S.; McNulty, I. Dichroic coherent diffractive imaging. *Proc. Natl. Acad. Sci. USA* **2011**, *108*, 13393–13398.
25. Shi, X.; Fischer, P.; Neu, V.; Elefant, D.; Lee, J.; Shapiro, D.; Farmand, M.; Tyliczszak, T.; Shiu, H.W.; Marchesini, S.; et al. Soft x-ray ptychography studies of nanoscale magnetic and structural correlations in thin SmCo_5 films. *Appl. Phys. Lett.* **2016**, *108*, 094103.
26. Huang, X.; Nelson, J.; Steinbrener, J.; Kirz, J.; Turner, J.J.; Jacobsen, C. Incorrect support and missing center tolerances of phasing algorithms. *Opt. Express* **2010**, *18*, 26441–26449.
27. Tripathi, A.; Shpyrko, O.; McNulty, I.; McNulty, I.; Eyberger, C.; Lai, B. Influence of Noise and Missing Data on Reconstruction Quality in Coherent X-ray Diffractive Imaging. In *AIP Conference Proceedings*; AIP: New York, NY, USA, 2011; Volume 1365, pp. 305–308.
28. Fienup, J.; Wackerman, C. Phase-retrieval stagnation problems and solutions. *JOSA A* **1986**, *3*, 1897–1907.
29. Marchesini, S. Invited article: A unified evaluation of iterative projection algorithms for phase retrieval. *Rev. Sci. Instrum.* **2007**, *78*, 011301.
30. Fienup, J.R. Phase retrieval algorithms: A comparison. *Appl. Opt.* **1982**, *21*, 2758–2769.
31. Marchesini, S.; He, H.; Chapman, H.N.; Hau-Riege, S.P.; Noy, A.; Howells, M.R.; Weierstall, U.; Spence, J.C. X-ray image reconstruction from a diffraction pattern alone. *Phys. Rev. B* **2003**, *68*, 140101.
32. Wilhelm, H.; Baenitz, M.; Schmidt, M.; Rößler, U.; Leonov, A.; Bogdanov, A. Precursor phenomena at the magnetic ordering of the cubic helimagnet FeGe. *Phys. Rev. Lett.* **2011**, *107*, 127203.
33. Moskvina, E.; Grigoriev, S.; Dyadkin, V.; Eckerlebe, H.; Baenitz, M.; Schmidt, M.; Wilhelm, H. Complex chiral modulations in FeGe close to magnetic ordering. *Phys. Rev. Lett.* **2013**, *110*, 077207.
34. Yu, X.Z.; Kanazawa, N.; Onose, Y.; Kimoto, K.; Zhang, W.; Ishiwata, S.; Matsui, Y.; Tokura, Y. Near room-temperature formation of a skyrmion crystal in thin-films of the helimagnet FeGe. *Nat. Mater.* **2011**, *10*, 106–109.
35. Huang, S.; Chien, C. Extended skyrmion phase in epitaxial FeGe (111) thin films. *Phys. Rev. Lett.* **2012**, *108*, 267201.
36. Kanazawa, N.; Kubota, M.; Tsukazaki, A.; Kozuka, Y.; Takahashi, K.; Kawasaki, M.; Ichikawa, M.; Kagawa, F.; Tokura, Y. Discretized topological Hall effect emerging from skyrmions in constricted geometry. *Phys. Rev. B* **2015**, *91*, 041122.
37. Kanazawa, N.; White, J.; Rønnow, H.M.; Dewhurst, C.; Fujishiro, Y.; Tsukazaki, A.; Kozuka, Y.; Kawasaki, M.; Ichikawa, M.; Kagawa, F.; et al. Direct observation of anisotropic magnetic field response of the spin helix in FeGe thin films. *Phys. Rev. B* **2016**, *94*, 184432.
38. Zhang, S.; Stasinopoulos, I.; Lancaster, T.; Xiao, F.; Bauer, A.; Rucker, F.; Baker, A.; Figueroa, A.; Salman, Z.; Pratt, F.; et al. Room-temperature helimagnetism in FeGe thin films. *Sci. Rep.* **2017**, *7*, doi:10.1038/s41598-017-00201-z.

39. Ahmed, A.S.; Rowland, J.; Esser, B.D.; Dunsiger, S.; McComb, D.W.; Randeria, M.; Kawakami, R.K. Chiral Bobber Formation in Epitaxial FeGe/Si (111) Films. *arXiv* **2017**, arXiv:1706.08248.
40. Gallagher, J.; Meng, K.; Brangham, J.; Wang, H.; Esser, B.; McComb, D.; Yang, F. Robust Zero-Field Skyrmion Formation in FeGe Epitaxial Thin Films. *Phys. Rev. Lett.* **2017**, *118*, 027201.
41. Bak, P.; Jensen, M.H. Theory of helical magnetic structures and phase transitions in MnSi and FeGe. *J. Phys. C Solid State Phys.* **1980**, *13*, L881.
42. Adams, T.; Mühlbauer, S.; Pfleiderer, C.; Jonietz, F.; Bauer, A.; Neubauer, A.; Georgii, R.; Böni, P.; Keiderling, U.; Everschor, K.; et al. Long-range crystalline nature of the skyrmion lattice in MnSi. *Phys. Rev. Lett.* **2011**, *107*, 217206.
43. Seki, S.; Kim, J.H.; Inosov, D.; Georgii, R.; Keimer, B.; Ishiwata, S.; Tokura, Y. Formation and rotation of skyrmion crystal in the chiral-lattice insulator Cu₂OSeO₃. *Phys. Rev. B* **2012**, *85*, 220406.
44. Yu, X.Z.; Onose, Y.; Kanazawa, N.; Park, J.; Han, J.; Matsui, Y.; Nagaosa, N.; Tokura, Y. Real-space observation of a two-dimensional skyrmion crystal. *Nature* **2010**, *465*, 901–904.
45. Chapman, J. The investigation of magnetic domain structures in thin foils by electron microscopy. *J. Phys. D Appl. Phys.* **1984**, *17*, 623.
46. Jiang, W.; Zhang, W.; Yu, G.; Jungfleisch, M.B.; Upadhyaya, P.; Somaini, H.; Pearson, J.E.; Tserkovnyak, Y.; Wang, K.L.; Heinonen, O.; et al. Mobile Néel skyrmions at room temperature: Status and future. *AIP Adv.* **2016**, *6*, 055602.
47. Pollard, S.D.; Garlow, J.A.; Yu, J.; Wang, Z.; Zhu, Y.; Yang, H. Observation of stable Néel skyrmions in cobalt/palladium multilayers with Lorentz transmission electron microscopy. *Nat. Commun.* **2017**, *8*, doi:10.1038/ncomms14761.
48. Romming, N.; Hanneken, C.; Menzel, M.; Bickel, J.E.; Wolter, B.; von Bergmann, K.; Kubetzka, A.; Wiesendanger, R. Writing and deleting single magnetic skyrmions. *Science* **2013**, *341*, 636–639.
49. Fert, A.; Cros, V.; Sampaio, J. Skyrmions on the track. *Nat. Nanotechnol.* **2013**, *8*, 152–156.
50. Chen, G.; Mascaraque, A.; N'Diaye, A.T.; Schmid, A.K. Room temperature skyrmion ground state stabilized through interlayer exchange coupling. *Appl. Phys. Lett.* **2015**, *106*, 242404.
51. Kézsmárki, I.; Bordács, S.; Milde, P.; Neuber, E.; Eng, L.; White, J.; Rønnow, H.M.; Dewhurst, C.; Mochizuki, M.; Yanai, K.; et al. Néel-type skyrmion lattice with confined orientation in the polar magnetic semiconductor GaV₄S₈. *Nat. Mater.* **2015**, *14*, 1116–1122.
52. Fujima, Y.; Abe, N.; Tokunaga, Y.; Arima, T. Thermodynamically stable skyrmion lattice at low temperatures in a bulk crystal of lacunar spinel GaV₄Se₈. *Phys. Rev. B* **2017**, *95*, 180410.
53. Bordács, S.; Butykai, A.; Szigeti, B.; White, J.; Cubitt, R.; Leonov, A.; Widmann, S.; Ehlers, D.; von Nidda, H.A.K.; Tsurkan, V.; et al. Equilibrium Skyrmion Lattice Ground State in a Polar Easy-plane Magnet. *Sci. Rep.* **2017**, *7*, 7584.
54. Kurumaji, T.; Nakajima, T.; Ukleev, V.; Feoktystov, A.; Arima, T.H.; Kakurai, K.; Tokura, Y. Néel-Type Skyrmion Lattice in the Tetragonal Polar Magnet VOSe₂O₅. *Phys. Rev. Lett.* **2017**, *119*, 237201.
55. Liu, H.; Xu, Z.; Zhang, X.; Wu, Y.; Guo, Z.; Tai, R. Effects of missing low-frequency information on ptychographic and plane-wave coherent diffraction imaging. *Appl. Opt.* **2013**, *52*, 2416–2427.
56. Van Heel, M.; Schatz, M. Fourier shell correlation threshold criteria. *J. Struct. Biol.* **2005**, *151*, 250–262.
57. Banterle, N.; Bui, K.H.; Lemke, E.A.; Beck, M. Fourier ring correlation as a resolution criterion for super-resolution microscopy. *J. Struct. Biol.* **2013**, *183*, 363–367.
58. Steinbrener, J.; Nelson, J.; Huang, X.; Marchesini, S.; Shapiro, D.; Turner, J.J.; Jacobsen, C. Data preparation and evaluation techniques for x-ray diffraction microscopy. *Opt. Express* **2010**, *18*, 18598–18614.
59. Wilke, R.; Vassholz, M.; Salditt, T. Semi-transparent central stop in high-resolution X-ray ptychography using Kirkpatrick–Baez focusing. *Acta Crystallogr. Sect. A Found. Crystallogr.* **2013**, *69*, 490–497.
60. He, H.; Marchesini, S.; Howells, M.; Weierstall, U.; Hembree, G.; Spence, J.C. Experimental lensless soft-X-ray imaging using iterative algorithms: Phasing diffuse scattering. *Acta Crystallogr. Sect. A Found. Crystallogr.* **2003**, *59*, 143–152.
61. Yamasaki, Y.; Sudayama, T.; Okamoto, J.; Nakao, H.; Kubota, M.; Murakami, Y. Diffractometer for small angle resonant soft X-ray scattering under magnetic field. *J. Phys. Conf. Ser.* **2013**, *425*, 132012.
62. Hannon, J.; Trammell, G.; Blume, M.; Gibbs, D. X-ray resonance exchange scattering. *Phys. Rev. Lett.* **1988**, *61*, 1245.

63. Shibata, K.; Iwasaki, J.; Kanazawa, N.; Aizawa, S.; Tanigaki, T.; Shirai, M.; Nakajima, T.; Kubota, M.; Kawasaki, M.; Park, H.; et al. Large anisotropic deformation of skyrmions in strained crystal. *Nat. Nanotechnol.* **2015**, *10*, 589–592.
64. Eisebitt, S.; Lörger, M.; Eberhardt, W.; Lüning, J.; Stöhr, J.; Rettner, C.; Hellwig, O.; Fullerton, E.; Denbeaux, G. Polarization effects in coherent scattering from magnetic specimen: Implications for X-ray holography, lensless imaging, and correlation spectroscopy. *Phys. Rev. B* **2003**, *68*, 104419.
65. Martin, A.V.; Wang, F.; Loh, N.; Ekeberg, T.; Maia, F.R.; Hantke, M.; van der Schot, G.; Hampton, C.Y.; Sierra, R.G.; Aquila, A.; et al. Noise-robust coherent diffractive imaging with a single diffraction pattern. *Opt. Express* **2012**, *20*, 16650–16661.
66. Lewis, J. Fast normalized cross-correlation. In *Vision Interface; Canadian Image Processing and Pattern Recognition Society: Quebec, QC, Canada, 1995; Volume 10*, pp. 120–123.



© 2018 by the authors. Licensee MDPI, Basel, Switzerland. This article is an open access article distributed under the terms and conditions of the Creative Commons Attribution (CC BY) license (<http://creativecommons.org/licenses/by/4.0/>).